Some mathematical models for flagellar activation mechanisms

François Alouges, Irene Anello, Antonio Desimone, Aline Lefebvre-Lepot, Jessie Levillain

Some mathematical models for flagellar activation mechanisms

François Alouges[1], Irene Anello[2], Antonio DeSimone[2], Aline Lefebvre-Lepot[3], and Jessie Levillain[4]

[1]Centre Borelli, ENS Paris-Saclay, CNRS, Université Paris-Saclay, 4 avenue des sciences, 91190 Gif-sur-Yvette, France, Institut Universitaire de France (IUF)
[2]Scuola Internazionale Superiore di Studi Avanzati, via Bonomea 265, I-34136 Trieste, Italy
[3]CNRS, Fédération de Mathématiques de CentraleSupélec, 9, rue Joliot Curie, 91190 Gif-sur-Yvette
[4]CMAP, CNRS, École polytechnique, Institut Polytechnique de Paris , route de Saclay, 91120 Palaiseau, France

September 10, 2024

Abstract

This paper focuses on studying a model for molecular motors responsible for the bending of the axoneme in the flagella of microorganisms. The model is a coupled system of partial differential equations inspired by [16, 18, 6], incorporating two rows of molecular motors between microtubules filaments. Existence and uniqueness of a solution is proved, together with the presence of a supercritical Hopf bifurcation. Additionally, numerical simulations are provided to illustrate the theoretical results. A brief study on the generalization to N-rows is also included.

1 Introduction

Cilia and flagella are active slender organelles employed by eukaryotic cells to swim through viscous fluid [27]. They exploit hydrodynamic friction to induce self-propulsion and show a characteristic non-reciprocal periodic motion in their dynamics [9, 10]. This enables them to move without relying on inertial forces, i.e., at a low Reynolds number [22]. Pioneering works ([20, 11, 26, 3, 4, 5]) established that some form of internal activity along the flagellum is necessary in order to have sustained oscillations.

This internal activity is present in all cilia and flagella due to their common internal structure, the axoneme. The axoneme consists of nine pairs of protofilaments called microtubules. It is an active structure due to the molecular motors located between neighboring microtubule pairs. These molecular motors are attached to one microtubule pair and walk along the adjacent pair, creating local sliding between contiguous microtubule pairs. This mechanism, which is fueled by the conversion of chemical energy (ATP) into mechanical work, creates bending along the filament [25].

The three-dimensional structure of the axoneme can be modeled as two planar filaments, with motors attached to the top filament exerting force on the fixed bottom filament ([6],[16],[17]). Since we are interested in the emergence of mesoscopic order in the axoneme from the uncoordinated activity of many independent molecular motors, we consider a portion of the filaments of arc-length of the order of 10ℓ, where ℓ is a sub-micron length scale defined by the periodic microtubule structure (specifically, the typical inter-dynein spacing is 24 nm, see [13]). Over this length scale, the filaments can be considered as rigid.

Throughout this paper, we will call the one-row model the system composed of a single row of motors between two filaments. In this work, we extend the one-row model by introducing a second row of molecular motors, as in Figure 1(b). We call this new framework, which symmetrizes the previous model, the two-row model. We also present a more comprehensive N-row model, where N corresponds to the number of motor rows.

To study the two-row model, we generalize the stochastic model proposed in [16]. Each motor is anchored to one of two filament pairs, pair 1 or pair 2, and has two identical heads, e.g. head A and head B, each of them being either bound or unbound to the opposite filament. The motor has two different chemical states, state 1, where head A is bound and head B is unbound, or state 2, where the opposite holds. In this model, both heads cannot be unbound (or bound) at the same time. Between the pair of filaments, passive elastic and viscous elements resist the motion; they are modeled by the positive constants k and η, respectively.

Each state $i = 1, 2$ is defined by its potential energy $W_i(\xi)$ at position $\xi \in \mathbb{R}$. The transition rates, $\omega_i(\xi) = \omega_{ij}(\xi)$ with $i, j = 1, 2$ and $i \neq j$, represent the probability per unit time for a motor to switch between state i to state j. Moreover, since the filament is a periodic structure, W_i and ω_i are periodic functions with period ℓ. As ATP provides the energy for the motor to change states, the transition rates depend on its concentration Ω. A detailed explanation of this is available in [15].

In the limit of an infinite system of motors, we introduce $P_i(\xi, t)$ as the probability density that a motor anchored to tubule pair i is in state 1 at position ξ and time t. To obtain the probability density that a motor anchored to tubule pair i is in state 2, one must compute $1/\ell - P_i$. The shift between the moving and the non-moving filament is measured by $x(t)$, with velocity $v(t) = \frac{d}{dt}x(t)$.

Let $P(\xi, t) = P_1(\xi, t)$ and $Q(\xi, t) = P_2(\xi + x(t), t)$. Then, we obtain (see

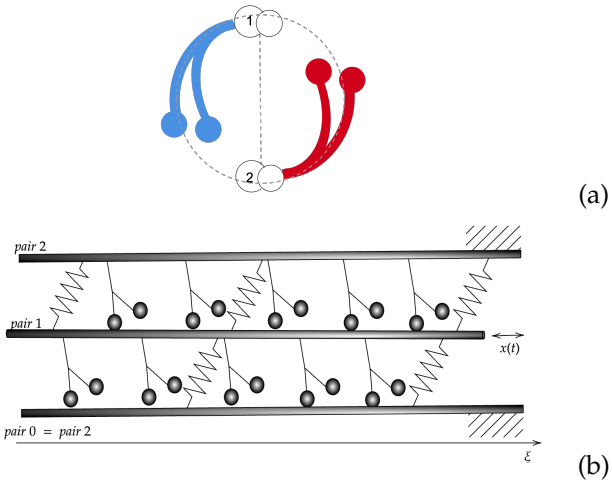

Figure 1: (a) Cross section of the partial axoneme with two opposite microtubule pairs. (b) Side view of the partial axoneme with two opposite microtubule pairs.

section 2) the following system of equations, for $\xi \in [0, \ell]$ and $t > 0$:

$$\begin{cases} \dfrac{\partial P}{\partial t}(\xi,t) + v(t)\dfrac{\partial P}{\partial \xi}(\xi,t) = -(\omega_1(\xi)+\omega_2(\xi))P(\xi,t) + \dfrac{\omega_2(\xi)}{\ell}, \\ \dfrac{\partial Q}{\partial t}(\xi,t) - v(t)\dfrac{\partial Q}{\partial \xi}(\xi,t) = -(\omega_1(\xi)+\omega_2(\xi))Q(\xi,t) + \dfrac{\omega_2(\xi)}{\ell}, \\ v(t) = \dfrac{1}{2\eta}\left(\displaystyle\int_0^\ell (P(\xi,t)-Q(\xi,t))\partial_\xi \Delta W(\xi) d\xi - 2kx(t)\right), \\ P(0,t) = P(\ell,t), \quad Q(0,t) = Q(\ell,t), \end{cases} \tag{1}$$

where $\omega_i = \omega_i(\xi;\Omega)$ and $\Delta W(\xi) = W_2(\xi) - W_1(\xi)$ are ℓ-periodic. As one can see in Figure 1(b), pair 0 and pair 2 are the same and they are both fixed.

The goal of this paper is twofold. On the one hand, we rigorously prove an existence and uniqueness result for the solution of (1). Furthermore, we show the existence of a Hopf bifurcation for that same system when reasonable formulas are taken for potentials W_i and transition rates ω_i, depending on the ATP concentration via Ω.

Moreover, we provide the reader with numerical simulations of (1), where an upwind scheme is employed to solve both transport equations. The numerical method is then extended to the more realistic N-row model.

Before stating the theoretical results, we point out that we assume (see [6, 12]),

$$\omega_1(\xi;\Omega) + \omega_2(\xi;\Omega) = a_0(\Omega), \tag{2}$$

where $a_0(\Omega) > 0$. Let us define $C^1_\#([0,\ell])$ as the set of restrictions to $[0,\ell]$ of C^1 and periodic functions over $\mathbb{R}$, then the first theorem reads as follows:

Theorem 1.1 (Existence and uniqueness)**.** *Let us fix $\ell > 0$. Assume $\omega_1(\xi;\Omega)$ and $\omega_2(\xi;\Omega)$ as in* (2)*. Moreover, assume ω_2 and ΔW to be at least $C^1_\#([0,\ell])$. If the initial data $P(\xi,0)$ and $Q(\xi,0)$ are $C^1_\#([0,\ell])$ and $x(0)=0$, then the system of equations* (1)*, admits a unique solution P, $Q \in C^1([0,\ell]\times\mathbb{R}_+)$, with $\xi \mapsto P(\xi,\cdot)$ and $\xi \mapsto Q(\xi,\cdot)$ in $C^1_\#([0,\ell])$, and $x \in C^1(\mathbb{R}_+)$.*

For the second result we chose $\Delta W(\xi) = U\cos\left(\dfrac{2\pi\xi}{\ell}\right)$, as in [6]. Moreover, since the two motor heads are identical, then $\omega_2(\xi) = \omega_1(\xi+\ell/2)$. Taking the transition rates' periodicity into account, we use the following Fourier expansion

$$\omega_2(\xi;\Omega) = \frac{a_0(\Omega)}{2} + \sum_{n=2k+1,\, k\geq 0} \left(a_n(\Omega)\cos\frac{2n\pi\xi}{\ell} + b_n(\Omega)\sin\frac{2n\pi\xi}{\ell}\right), \quad (3)$$

with $a_n(\Omega)$ and $b_n(\Omega)$ real coefficients.

Theorem 1.2 (Hopf bifurcation)**.** *In addition to the hypothesis above, assume that $a_0(\Omega) = a_0^0\Omega^{\alpha_0}$, $a_1(\Omega) = a_1^0\Omega^{\alpha_1}$, $b_1(\Omega) = b_1^0\Omega^{\alpha_1}$ for $a_1^0, b_1^0 \in \mathbb{R}$ and $\alpha_0, \alpha_1, a_0^0, \Omega \in \mathbb{R}_+$. Furthermore, let us define*

$$\tau(\Omega) := -\frac{1}{4}(2a_0^0\Omega^{\alpha_0} + \frac{\zeta\ell}{\pi} + 2\lambda\frac{a_1^0}{a_0^0\ell}\Omega^{\alpha_1-\alpha_0}), \quad (4)$$

with $\zeta = 2\pi k/\eta\ell$ and $\lambda = 2\pi^2 U/\eta\ell$. Suppose there exists $\Omega_0 \in \mathbb{R}_+$ such that $\tau(\Omega_0) = 0$ and $\tau'(\Omega_0) > 0$, then the solutions $P(\xi,t;\Omega)$, $Q(\xi,t;\Omega)$ and $x(t;\Omega)$ of the system (1) *show a super-critical Hopf bifurcation in time near the bifurcation value Ω_0 and near the fixed point*

$$(P_{eq}(\xi;\Omega), Q_{eq}(\xi;\Omega), x_{eq}(\Omega)) = \left(\frac{\omega_2(\xi;\Omega)}{a_0(\Omega)l}, \frac{\omega_2(\xi;\Omega)}{a_0(\Omega)l}, 0\right).$$

In particular, the fixed point is asymptotically stable for $\Omega < \Omega_0$, and unstable for $\Omega > \Omega_0$. Moreover there exists an asymptotically stable periodic orbit for $\Omega > \Omega_0$ with radius

$$\rho = \sqrt{-\frac{(\Omega-\Omega_0)\tau'(\Omega_0)}{\tilde{\tau}}} + o\left(\sqrt{\Omega-\Omega_0}\right), \quad (5)$$

where $\tilde{\tau} = -\dfrac{3\pi\zeta}{4\ell}\left(\dfrac{\pi a_0^0\Omega_0^{\alpha_0} + \ell\zeta}{\pi a_0^0\Omega_0^{\alpha_0} + 2\ell\zeta}\right)$, $\tilde{\tau} < 0$.

The methods introduced to prove the theorems can be also used to demonstrate similar results for the one-row model, and might prove useful to consider the general N-row structure.

The next section presents the two-row model and proves Theorems 1.1 and 1.2, with numerical simulations confirming these results. The final section explores new questions by extending the model to an N-row structure.

2 The two-row model

2.1 Motivation

In this section we focus on the two-row model, from both theoretical and numerical perspectives.

The two-row model serves the purpose of symmetrizing the one-row model. In the one-row model [16], even without any external force, the moving filaments experiences a non-zero equilibrium displacement $x(t) = x_{eq}$, which disrupts axonemal symmetry and causes bending at rest. Jülicher and Camalet mentioned this issue in [6], solving it by choosing symmetrical potentials, as in our case, and symmetrical transition rates, namely $|\omega_i(\xi + l/2)| = |\omega_i(-\xi + l/2)|$, with $\xi \in [0, \ell]$. Instead, in this work, we model non-symmetrical transition rates and introduce a second row of molecular motors, producing a zero equilibrium $x_{eq} = 0$ at rest.

The two-row model is a simplified version of the axoneme that acts like its two-dimensional projection ([24, 7]), forming a cylinder with only two microtubule pairs linked by two motor rows, as shown in Figure 1(a). Moreover, this model is a first step to the N-row model presented in section 3, where N corresponds to the quantity of motor rows.

Despite lacking additional sliding regulation components, the model demonstrates that dyneins can synchronize and self-regulate to create alternating sliding on both sides of the axoneme. This matches, in particular, with the curvature regulation hypothesis called steady dynein loading [2, 14, 30] in which axonemal curvature is created without any inhibition mechanism transmitted along the system.

2.2 Model structure

We now derive in detail the system (1), which is depicted in Figure 1(b). We consider three pairs of filaments, numbered from 0 to 2. The pairs 0 and 2 are identical, and fixed, while the central pair 1, may move. We call $x(t)$ its displacement, and $v(t) = \frac{d}{dt}x(t)$ its velocity. We define $P_1(\xi, t)$ and $P_2(\xi, t)$ as the probabilities for the motors to be in state one at position ξ and time t, when attached to the pair 1 (bottom row) or to the pair 2 (top row), respectively. We assume that the sum of the transition rates is uniform, as in (2), and obtain two transport equations for $\xi \in [0, \ell]$ and $t > 0$:

$$\begin{cases} \dfrac{\partial P_1}{\partial t}(\xi, t) + v(t)\dfrac{\partial P_1}{\partial \xi}(\xi, t) = -a_0(\Omega)P_1(\xi, t) + \dfrac{\omega_2(\xi; \Omega)}{\ell}, \\ \dfrac{\partial P_2}{\partial t}(\xi, t) = -a_0(\Omega)P_2(\xi, t) + \dfrac{\omega_2(\xi - x(t); \Omega)}{\ell}. \end{cases} \tag{6}$$

Additionally, the force balance equation on the central filament reads:

$$f_{ext} - 2\eta v - 2kx + f_{mot} = 0, \tag{7}$$

where f_{ext} is the external force applied on the central filament, and f_{mot} is the active force exerted by the motors, which is given by

$$f_{mot}(t) = \int_0^\ell (P_1(\xi,t)\partial_\xi \Delta W(\xi) - P_2(\xi,t)\partial_\xi \Delta W(\xi - x(t)))d\xi. \tag{8}$$

Here, kx and ηv represent the elastic and viscous resistances, respectively. For the purpose of our work, we do not consider any external forcing, which means $f_{ext} = 0$. Let $P(\xi,t) = P_1(\xi,t)$ and $Q(\xi,t) = P_2(\xi + x(t),t)$. Then, (6) becomes

$$\begin{cases} \dfrac{\partial P}{\partial t}(\xi,t) + v(t)\dfrac{\partial P}{\partial \xi}(\xi,t) = -a_0(\Omega)P(\xi,t) + \dfrac{\omega_2(\xi)}{\ell}, \\ \dfrac{\partial Q}{\partial t}(\xi,t) - v(t)\dfrac{\partial Q}{\partial \xi}(\xi,t) = -a_0(\Omega)Q(\xi,t) + \dfrac{\omega_2(\xi)}{\ell}. \end{cases} \tag{9}$$

The periodicity of P_1 and P_2, enables us to rewrite the motor force as

$$f_{mot}(t) = \int_0^\ell (P(\xi,t) - Q(\xi,t))\partial_\xi \Delta W(\xi)d\xi\,,$$

and obtain, from (7),

$$v(t) = \dot{x}(t) = \frac{1}{2\eta}\left(\int_0^\ell (P(\xi,t) - Q(\xi,t))\partial_\xi \Delta W(\xi)d\xi - 2kx(t)\right). \tag{10}$$

Finally, we recover the system of equations (1), which will then be studied both theoretically and numerically, before generalizing it to an arbitrary number of layers N.

2.3 Proof of Theorem 1.1 (existence and uniqueness)

The proof follows a classical scheme in two steps: we first show local existence of the solution in time, and then extend it to $\mathbb{R}_+$.

Step 1: local existence. Let $T > 0$ be a time to be chosen afterwards and define the map $\psi : C^0([0,T]) \to C^0([0,T])$ as $\psi[x(\cdot)](t) = \displaystyle\int_0^t F[x(\cdot)](s)\,ds$, where

$$F[x(\cdot)](s) = \frac{1}{2\eta}\int_0^\ell (P_x(\xi,s) - Q_x(\xi,s))\partial_\xi \Delta W(\xi)d\xi - \frac{k}{\eta}x(s), \tag{11}$$

and the functions $P_x(\xi,t)$ and $Q_x(\xi,t)$ are defined as the solutions of (9) and $v(t)=\dot{x}(t)$. Notice that P_x and Q_x are explicitly given in their integral form by

$$P_x(\xi,t)=e^{-a_0t}P(\xi-x(t)+x(0),0)+\frac{e^{-a_0t}}{\ell}\int_0^t e^{a_0s}\omega_2(\xi+x(s)-x(t))\,ds, \quad (12)$$

and

$$Q_x(\xi,t)=e^{-a_0t}Q(\xi+x(t)-x(0),0)+\frac{e^{-a_0t}}{\ell}\int_0^t e^{a_0s}\omega_2(\xi-x(s)+x(t))\,ds, \quad (13)$$

which remain well-defined when x is only in $C^0([0,T])$.

Notice that $(\tilde{x},P_{\tilde{x}},Q_{\tilde{x}})$ is a solution of the system (9, 10) if and only if $\tilde{x}(t)$ is a fixed point of ψ, i.e. $\psi[\tilde{x}(\cdot)]=\tilde{x}(\cdot)$. In order to proceed, we prove that $\psi:C^0([0,T])\to C^0([0,T])$ is a strict contraction for T sufficiently small.

Let us take two functions x_1 and x_2 in $C^0([0,T])$, with $x_1(0)=x_2(0)=0$ and with the corresponding P_{x_1}, Q_{x_1} and P_{x_2}, Q_{x_2} defined by the integral formulations (12, 13). The initial conditions are identical $P_{x_1}(\xi,0)=P_{x_2}(\xi,0)=P(\xi)$ and $Q_{x_1}(\xi,0)=Q_{x_2}(\xi,0)=Q(\xi)$. We want to estimate the quantity

$$\psi[x_1(\cdot)](t)-\psi[x_2(\cdot)](t)=\int_0^t F[x_1(\cdot)](s)-F[x_2(\cdot)](s)\,ds. \quad (14)$$

Using (11), we get

$$\begin{aligned}F[x_1(\cdot)](s)-F[x_2(\cdot)](s)=\frac{1}{2\eta}\Bigg(\int_0^\ell \Big(P_{x_1}(\xi,s)-P_{x_2}(\xi,s)\\ -\big(Q_{x_1}(\xi,s)-Q_{x_2}(\xi,s)\big)\Big)\partial_\xi\Delta W(\xi)d\xi\Bigg)-\frac{k}{\eta}(x_1(s)-x_2(s)).\end{aligned} \quad (15)$$

Now, we have from (12)

$$\begin{aligned}P_{x_1}(\xi,t)-P_{x_2}(\xi,t)=e^{-a_0t}(P_{x_1}(\xi-x_1(t),0)-P_{x_2}(\xi-x_2(t),0))\\ +\frac{e^{-a_0t}}{\ell}\int_0^t e^{a_0s}(\omega_2(\xi+x_1(s)-x_1(t))-\omega_2(\xi+x_2(s)-x_2(t))\,ds.\end{aligned} \quad (16)$$

We have the estimate

$$\begin{aligned}&\|P_{x_1}(t,\xi)-P_{x_2}(t,\xi)\|_{L_t^\infty L_\xi^\infty}\\ &\le\|\partial_\xi P\|_{L_\xi^\infty}\|x_1(t)-x_2(t)\|_{L_t^\infty}\\ &\quad+\frac{1}{\ell}\left\|\int_0^t e^{a_0(s-t)}\|\partial_\xi\omega_2\|_{L_\xi^\infty}|x_1(s)-x_1(t)-x_2(s)+x_2(t))|\,ds\right\|_{L_t^\infty}\\ &\le\left(\|\partial_\xi P\|_{L_\xi^\infty}+\frac{2}{a_0\ell}\|\partial_\xi\omega_2\|_{L_\xi^\infty}\right)\|x_1(t)-x_2(t)\|_{L_t^\infty},\end{aligned}$$

The same goes for the difference $Q_{x_1}(\xi,t) - Q_{x_2}(\xi,t)$, and we deduce

$$\|P_{x_1}(t,\xi) - P_{x_2}(t,\xi) - Q_{x_1}(t,\xi) + Q_{x_2}(t,\xi)\|_{L^\infty_t L^\infty_\xi} \leq C_1 \|x_1(t) - x_2(t)\|_{L^\infty_t}. \quad (17)$$

with $C_1 = 4\max\left\{\|\partial_\xi Q\|_{L^\infty_\xi}, \|\partial_\xi P\|_{L^\infty_\xi}, \frac{2}{a_0\ell}\|\partial_\xi \omega_2\|_{L^\infty_\xi}\right\}$.

We now deduce from (15)

$$\|F[x_1(\cdot)] - F[x_2(\cdot)]\|_{L^\infty_t} \leq \left(\frac{C_1\ell}{2\eta}\|\partial_\xi \Delta W\|_{L^\infty_\xi} + \frac{k}{\eta}\right)\|x_1(t) - x_2(t)\|_{L^\infty_t}, \quad (18)$$

and obtain

$$\|\psi[x_1(\cdot)] - \psi[x_2(\cdot)]\|_{L^\infty_t} \leq C_2 T \|x_1 - x_2\|_{L^\infty_t}, \quad (19)$$

with $C_2 = \frac{C_1\ell}{2\eta}\|\partial_\xi \Delta W\|_{L^\infty_\xi} + k/\eta$.

Taking $T = \frac{1}{2C_2}$, this proves that ψ is a contraction, as claimed. Then, there exists a unique fixed point $\tilde{x}(\cdot) \in C^0([0,T])$ which satisfies (10).

Step 2: global solutions. The previous construction can be extended as long as P_x and Q_x remain bounded in $C^1([0,\ell])$ with respect to ξ and in $L^\infty(\mathbb{R}_+)$ with respect to t, as shown by the formulas for C_1 and C_2. But from (12, 13) we have

$$\|P_x(\cdot,t)\|_{C^1_\xi} \leq e^{-a_0 t}\|P\|_{C^1_\xi} + (1 - e^{-a_0 t})\frac{1}{a_0\ell}\|\omega_2\|_{C^1_\xi},$$

which shows that

$$\|P_x\|_{C^1_\xi, L^\infty_t} \leq \max\left(\|P\|_{C^1_\xi}, \frac{1}{a_0\ell}\|\omega_2\|_{C^1_\xi}\right),$$

and the same goes for Q_x. We thus obtain that there is a unique global solution $(x,\, P_x,\, Q_x)$ to (9, 10) for all time $t \geq 0$.

In fact, $x \in C^1(\mathbb{R}_+)$ and $P_x,\, Q_x \in C^1_\#([0,\ell] \times \mathbb{R}_+)$, with $\xi \mapsto P(\xi,\cdot)$ and $\xi \mapsto Q(\xi,\cdot)$ in $C^1_\#([0,\ell])$, as shown by the following bootstrap argument: From equations (12, 13), we know that P_x and Q_x are continuous in time, which enables us to deduce that $F[x(\cdot)] \in C^0(\mathbb{R}_+)$. Therefore, $\psi[x(\cdot)] \in C^1(\mathbb{R}_+)$. But, since $x = \psi[x(\cdot)]$, we deduce that $x \in C^1(\mathbb{R}_+)$. Re-using equations (12, 13), we may then deduce that P_x and Q_x are in fact C^1 in time (and they actually have the minimal regularity of the initial conditions $P,\, Q$ and of ω_2).

2.4 Proof of Theorem 1.2 (Hopf bifurcation)

The functions $\xi \mapsto P(\xi,t)$ and $\xi \mapsto Q(\xi,t)$ are periodic with period l, and they can be then expanded in Fourier series

$$\begin{cases} P(\xi,t) = \dfrac{p_0(t)}{2} + \displaystyle\sum_{n>0}\left(p_n^c(t)\cos\frac{2n\pi\xi}{\ell} + p_n^s(t)\sin\frac{2n\pi\xi}{\ell}\right), \\ Q(\xi,t) = \dfrac{q_0(t)}{2} + \displaystyle\sum_{n>0}\left(q_n^c(t)\cos\frac{2n\pi\xi}{\ell} + q_n^s(t)\sin\frac{2n\pi\xi}{\ell}\right). \end{cases} \quad (20)$$

We insert this expansion and the one for the transition rates (3) into the system (1). By matching same order terms, we get an infinite number of ordinary differential equations for the coefficients of P and Q. Namely, for $n = 0$ we get two decoupled equations for p_0 and q_0:

$$\dot{p_0}(t) = -a_0(\Omega)p_0(t) + a_0(\Omega)/2\ell, \quad \dot{q_0}(t) = -a_0(\Omega)q_0(t) + a_0(\Omega)/2\ell. \tag{21}$$

For $n \neq 0$ we obtain:

$$\begin{cases} \dot{p_n^c}(t) + \frac{2\pi n}{\ell} v(t) p_n^s(t) = -a_0(\Omega)p_n^c(t) + a_n(\Omega)/\ell\,, \\ \dot{p_n^s}(t) - \frac{2\pi n}{\ell} v(t) p_n^c(t) = -a_0(\Omega)p_n^s(t) + b_n(\Omega)/\ell\,, \\ \dot{q_n^c}(t) - \frac{2\pi n}{\ell} v(t) q_n^s(t) = -a_0(\Omega)q_n^c(t) + a_n(\Omega)/\ell\,, \\ \dot{q_n^s}(t) + \frac{2\pi n}{\ell} v(t) q_n^c(t) = -a_0(\Omega)q_n^s(t) + b_n(\Omega)/\ell\,, \end{cases} \tag{22}$$

together with the force balance equation

$$2\eta\dot{x}(t) + 2kx(t) + \pi U(p_1^s - q_1^s) = 0\,. \tag{23}$$

Note that the coupling between the probabilities evolution and the force equilibrium equation takes place only for the first order coefficients. We are going to prove the existence of a Hopf bifurcation by treating order $n = 0$ first, then $n = 1$ and lastly $n > 1$. Combining all three results will complete the proof.

Step 1. Zeroth order coefficients. It is clear that (21) gives

$$p_0(t) = e^{-a_0 t}\left(p_0(0) - \frac{1}{2l}\right) + \frac{1}{2\ell}\,, \quad q_0(t) = e^{-a_0 t}\left(q_0(0) - \frac{1}{2l}\right) + \frac{1}{2\ell}\,,$$

and both converge to $\frac{1}{2\ell}$ exponentially fast.

Step 2. First order coefficients. We now prove the onset of oscillatory patterns for the first order coefficients $p_1^{c,s}(t)$, $q_1^{c,s}(t)$, and for the position $x(t)$.

From (22) and (23) we obtain a first-order five-dimensional ODE:

$$\begin{cases} \dot{p_1^c} = -a_0(\Omega)p_1^c + \big(\zeta x + \dfrac{\lambda}{2}(p_1^s - q_1^s)\big)p_1^s + \dfrac{a_1(\Omega)}{\ell}, \\ \dot{p_1^s} = -a_0(\Omega)p_1^s - \big(\zeta x + \dfrac{\lambda}{2}(p_1^s - q_1^s)\big)p_1^c + \dfrac{b_1(\Omega)}{\ell}, \\ \dot{q_1^c} = -a_0(\Omega)q_1^c - \big(\zeta x + \dfrac{\lambda}{2}(p_1^s - q_1^s)\big)q_1^s + \dfrac{a_1(\Omega)}{\ell}, \\ \dot{q_1^s} = -a_0(\Omega)q_1^s + \big(\zeta x + \dfrac{\lambda}{2}(p_1^s - q_1^s)\big)q_1^c + \dfrac{b_1(\Omega)}{\ell}, \\ \dot{x} = -\dfrac{\ell}{2\pi}\big(\zeta x + \dfrac{\lambda}{2}(p_1^s - q_1^s)\big)\,, \end{cases} \tag{24}$$

where $\zeta = 2\pi k/\eta\ell$ and $\lambda = 2\pi^2 U/\eta\ell$.

We linearize the system around its equilibrium point $p_{eq}(\Omega) = (p^c_{1,\mathrm{eq}}(\Omega), p^s_{1,\mathrm{eq}}(\Omega), q^c_{1,\mathrm{eq}}(\Omega), q^s_{1,\mathrm{eq}}(\Omega), x_{\mathrm{eq}}(\Omega))$, where

$$p^c_{1,eq} = q^c_{1,eq} = \frac{a_1(\Omega)}{a_0(\Omega)\ell}\,, \;\; p^s_{1,eq} = q^s_{1,eq} = \frac{b_1(\Omega)}{a_0(\Omega)\ell}\,, \;\; x_{eq} = 0\,.$$

We observe that the Jacobian matrix has five eigenvalues: three of them are equal to $-a_0(\Omega) < 0$ while the other two are of the form $\tau(\Omega) \pm \frac{1}{2\sqrt{\pi}} \sqrt{-2\zeta\ell a_0(\Omega) + \pi\,\tau^2(\Omega)}$, where $\tau(\Omega)$ is given by (4). Since, by hypothesis, there exists a real and positive $\Omega = \Omega_0$ such that $\tau(\Omega_0) = 0$, then $-2\zeta\ell a_0(\Omega_0) + \pi\,\tau^2(\Omega_0) < 0$, and we deduce that the pair of complex eigenvalues can be written as $\tau(\Omega) \pm i\omega(\Omega)$ where

$$\omega(\Omega) := -\frac{1}{2\sqrt{\pi}} \sqrt{2\zeta\ell a_0(\Omega) - \pi\,\tau^2(\Omega)}, \tag{25}$$

and they cross the imaginary axis at $\Omega = \Omega_0$.

In the following proposition, we are going to study the non-linear behavior of the vector field solution to (24) by exploiting the center manifold theorem; the orbit structure near the fixed point and Ω_0 is determined by the restriction of the non linear system to the center manifold. In particular, system (24) restricted to the center manifold will show a super-critical Hopf bifurcation near $p_{eq}(\Omega_0)$ and Ω_0.

Proposition 2.1 (First order coefficients)**.** *With the hypothesis of Theorem 1.2, the non-linear system* (24) *has a supercritical Hopf bifurcation near* $(p_{eq}(\Omega_0), \Omega_0)$.

Proof. **Change of variables.**
In the first part of the proof we restrict the dynamical system to the center manifold. To compute the latter, we bring the system to a more suitable formulation.

Let us first transform the fixed point of (24) to the origin. We define the new variables as

$$\delta p_1^c = p_1^c - p_{1,eq}^c,\ \delta p_1^s = p_1^s - p_{1,eq}^s,\ \delta q_1^c = q_1^c - q_{1,eq}^c,\ \delta q_1^s = q_1^s - q_{1,eq}^s.$$

We then use the following linear and invertible change of variables

$$r = \tfrac{a_1}{b_1}\delta p_1^c + \delta p_1^s, \quad s = \tfrac{a_1}{b_1}\delta q_1^c + \delta q_1^s, \quad z = \tfrac{1}{2}(\delta p_1^s + \delta q_1^s), \quad y = \tfrac{1}{2}(\delta p_1^s - \delta q_1^s),$$

and shorten the notation by taking $X = (r, s, z)^T$, and $Y = (y, x)^T$ to transform the system (24) into

$$\frac{d}{dt}\begin{pmatrix} X \\ Y \end{pmatrix} = \mathbb{M}(\Omega)\begin{pmatrix} X \\ Y \end{pmatrix} + \begin{pmatrix} G(X,Y) \\ F(X,Y) \end{pmatrix}, \tag{26}$$

where

$$\mathbb{M}(\Omega) = \begin{pmatrix} \mathbb{B}(\Omega) & 0 \\ 0 & \mathbb{A}(\Omega) \end{pmatrix}$$

is a block diagonal matrix. Since we assumed that $a_0(\Omega) = a_0^0\Omega^{\alpha_0}$, $a_1(\Omega) = a_1^0\Omega^{\alpha_1}$, $b_1(\Omega) = b_1^0\Omega^{\alpha_1}$ for $a_1^0 \in \mathbb{R}$ and $\alpha_0, \alpha_1, a_0^0, \Omega \in \mathbb{R}_+$, then for the linear part we have

$$\mathbb{B}(\Omega) = -a_0^0\Omega^{\alpha_0}\mathrm{Id}_{3,3}\,, \quad \mathbb{A}(\Omega) = \begin{pmatrix} -a_0^0\Omega^{\alpha_0} - \frac{\lambda}{\ell}\frac{a_1^0}{a_0^0}\Omega^{\alpha_1-\alpha_0} & -\frac{a_1^0}{a_0^0}\frac{\zeta}{\ell}\Omega^{\alpha_1-\alpha_0} \\ -\frac{\lambda\ell}{2\pi} & -\frac{\zeta\ell}{2\pi} \end{pmatrix}, \tag{27}$$

and the non linear part is defined as

$$G(X,Y) = (\zeta x + \lambda y) \begin{pmatrix} \frac{a_1^0}{b_1^0}(y+z) + \frac{b_1^0}{a_1^0}(-r+y+z) \\ \frac{a_1^0}{b_1^0}(y-z) + \frac{b_1^0}{a_1^0}(s+y-z) \\ -\frac{b_1^0}{a_1^0}\frac{(r-s-2y)}{2} \end{pmatrix},$$

and

$$F(X,Y) = (\zeta x + \lambda y) \begin{pmatrix} -\frac{b_1^0}{a_1^0}\frac{(r+s-2z)}{2} \\ 0 \end{pmatrix}. \tag{28}$$

Computation of the center manifold.

The center manifold can then be computed by using standard techniques (see [29], Chapter 20, Section 2). We start by rewriting the system in such a way that Ω_0 is moved to the origin through the change of variable $\delta\Omega = \Omega - \Omega_0$. As it is classical, we treat $\delta\Omega$ as a variable of the system. This means that we add the equation $\delta\dot{\Omega} = 0$ to the dynamical system and that the non linear part of the system includes all the products $\delta\Omega\, r$, $\delta\Omega\, s$, $\delta\Omega\, z$ etc.

Since the terms in the matrix $\mathbb{M}$ are nonlinear in Ω, we expand them as

$$(\Omega_0 + \delta\Omega)^\alpha = \Omega_0^\alpha + c(\alpha)\,\delta\Omega + O(\delta\Omega^{\,2}), \tag{29}$$

where $c(\alpha) = \alpha\Omega_0^{\alpha-1}$.

We insert the expansion (29) into the system (26), neglecting terms of order two in $\delta\Omega$ and getting

$$\frac{d}{dt}\begin{pmatrix} X \\ Y \\ \delta\Omega \end{pmatrix} = \mathbb{M}(\Omega_0)\begin{pmatrix} X \\ Y \\ 0 \end{pmatrix} + \begin{pmatrix} g(X,Y,\delta\Omega) \\ f(X,Y,\delta\Omega) \\ 0 \end{pmatrix}, \tag{30}$$

with

$$g(X,Y,\delta\Omega) = -a_0^0 c(\alpha_0)\delta\Omega X + G(X,Y)$$

and

$$f(X,Y,\delta\Omega) = -\begin{pmatrix} \left(a_0^0 c(\alpha_0) y + \frac{\lambda}{\ell}\frac{a_1^0}{a_0^0}c(\alpha_1-\alpha_0)\right)\delta\Omega\, y + \frac{\zeta}{\ell}c(\alpha_1-\alpha_0)\delta\Omega\, x \\ 0 \end{pmatrix} + F(X,Y).$$

We can define a center manifold as

$$W^c(0) = \{(X,Y,\delta\Omega) : X = \mathbf{h}(Y,\delta\Omega), |Y| < \varepsilon, |\delta\Omega\,| < \bar{\varepsilon}, \mathbf{h}(0,0) = 0,\ \nabla\mathbf{h}(0,0) = 0\},$$

for ε and $\bar{\varepsilon}$ sufficiently small and $\mathbf{h} = (h_1, h_2, h_3)$ smooth enough.

In order for $\mathbf{h}$ to be the center manifold for the system (30), the graph of $\mathbf{h}(Y, \delta\Omega)$ has to be invariant under the dynamics generated by (30). Hence, by plugging $\mathbf{h}$ into the system and compute its derivative, we get the following quasilinear differential equation

$$\nabla_Y \mathbf{h} \cdot (\mathbb{A}(\Omega_0)Y + f(\mathbf{h}, Y, \delta\Omega)) = \mathbb{B}(\Omega_0)\mathbf{h} + g(\mathbf{h}, Y, \delta\Omega). \tag{31}$$

The solution $\mathbf{h}(Y, \delta\Omega)$ of (31) can be approximated with a power series expansion up to any desired degree of accuracy. In our case we expand them up to order two defining

$$h_i(Y, \delta\Omega) := a_{i1}y^2 + a_{i2}yx + a_{i3}y\delta\Omega + a_{i4}x^2 + a_{i5}x\delta\Omega + a_{i6}\delta\Omega^2 + O(Y^3, \delta\Omega^3). \tag{32}$$

To completely determine (locally) the center manifold, we have to compute the coefficients a_{ij} knowing that the functions defined in (32) must solve (31). For the detailed computations, we refer the reader to Appendix 4.

Restricted to the center manifold, the original system (26) has the following form:

$$\frac{d}{dt}Y = \mathbb{A}(\Omega)Y + f(\mathbf{h}(Y), Y) + O(Y^3, \delta\Omega^3)\,. \tag{33}$$

A complete formula for $f(\mathbf{h}(Y), Y))$ in terms of $Y = (y, x)^T$ follows from our computations and reads

$$f(\mathbf{h}(Y), Y) = \begin{pmatrix} \dfrac{2\pi a_0^0 \ell(\lambda y + \zeta x)\left(\pi a_1^0 \Omega_0^{\alpha_1-\alpha_0}\left(\lambda^2 y^2 + \zeta^2 x^2\right) + \zeta a_0^0 \ell(\pi a_0^0 \Omega_0^{\alpha_0} - \zeta\ell)yx\right)}{\left(2\pi a_1^0 \lambda \Omega_0^{\alpha_1-\alpha_0} + \zeta a_0^0 \ell^2\right)\left(2\pi a_1^0 \lambda \Omega_0^{\alpha_1-\alpha_0} + a_0^0 \ell(\pi a_0^0 \Omega_0^{\alpha_0} - \zeta\ell)\right)} \\ 0 \end{pmatrix}.$$

Observe that $\tau(\Omega) \pm i\omega(\Omega)$ is the pair of conjugated eigenvalues of $\mathbb{A}(\Omega)$ and therefore we are in the hypothesis of the existence of a Hopf bifurcation for a two-dimensional system.

Normal form.

The next step is to bring system (33) into its normal form, from which we deduce the type of Hopf bifurcation that the system is attaining.

In order to proceed, we apply a further change of coordinates, such that $\mathbb{A}(\Omega)$ is transformed to its real Jordan form. Namely, we define the transformation matrix

$$\mathbb{P} = \begin{pmatrix} P_{11} & P_{12} \\ 1 & 0 \end{pmatrix},$$

where

$$P_{11} = \frac{\pi}{\lambda\ell}\left(\frac{a_1^0 \lambda \Omega_0^{\alpha_1-\alpha_0}}{a_0^0 \ell} + a_0^0 \Omega_0^{\alpha_0}\right) - \frac{\zeta}{2\lambda}$$

and

$$P_{12} = -\frac{1}{\lambda\ell}\sqrt{\pi\zeta\ell\left(a_0^0\Omega_0^{\alpha_0} - \frac{a_1^0\lambda\Omega_0^{\alpha_1-\alpha_0}}{a_0^0\ell}\right) - \left(\frac{\pi a_1^0 \lambda \Omega_0^{\alpha_1-\alpha_0}}{a_0^0\ell} + \pi a_0^0 \Omega_0^{\alpha_0}\right)^2 - \frac{\zeta^2\ell^2}{4}}.$$

The matrix $\mathbb{P}$ defines the new coordinates $Y = \mathbb{P}\tilde{Y}$ thanks to which equation (33) can be expressed in its normal form

$$\frac{d}{dt}\tilde{Y} = \begin{pmatrix} \tau(\Omega) & -\omega(\Omega) \\ \omega(\Omega) & \tau(\Omega) \end{pmatrix} \tilde{Y} + \mathbb{P}^{-1} f(\mathbf{h}(\mathbb{P}\tilde{Y}), \mathbb{P}\tilde{Y}) + O(Y^3, \delta\Omega^3). \tag{34}$$

To compute key properties of the system, such as the amplitude of the limit cycles, we change coordinates to the polar ones $\tilde{Y}^T = \rho(\sin(\theta), \cos(\theta))$, and get

$$\begin{cases} \dot{\rho}(t) = \tau'(\Omega_0)\delta\Omega\rho(t) + \tilde{\tau}\rho^3(t) + O(\delta\Omega^2\rho, \delta\Omega\rho^3), \\ \dot{\theta}(t) = \omega(\Omega_0) + \omega'(\Omega_0)\delta\Omega + \tilde{\omega}\rho^2(t) + O(\delta\Omega^2, \delta\Omega\rho^2). \end{cases}, \tag{35}$$

that is the normal form of (33) in polar coordinates around Ω_0.

The non linear part $\mathbb{P}^{-1} f(\mathbf{h}(\mathbb{P}\tilde{Y}), \mathbb{P}\tilde{Y})$ determines the constants $\tilde{\tau}$ and $\tilde{\omega}$. The first one is involved in the expression for the limit cycle amplitude, and we compute it using a well know formula (see [29], Chapter 20, Section 2). We obtain

$$\tilde{\tau} = -\frac{3\pi\zeta}{4\ell}\left(\frac{\pi a_0^0 \Omega_0^{\alpha_0} + \ell\zeta}{\pi a_0^0 \Omega_0^{\alpha_0} + 2\ell\zeta}\right)$$

Since $\tilde{\tau}$ is negative and

$$\tau'(\Omega_0) = -\frac{1}{2}\left(\frac{a_1^0\lambda\alpha_1 - \alpha_0\Omega^{\alpha_1-\alpha_0-1}}{a_0^0\ell} + \alpha_0 a_0^0 \Omega^{\alpha_0-1}\right),$$

is positive by hypothesis, the reduced system (33), and hence, the whole system (26), shows a supercritical Hopf bifurcation near the bifurcation parameter Ω_0.

In particular, for Ω sufficiently near and greater then Ω_0 there exists an asymptotically stable periodic orbit with radius as in (5). This finishes the proof of Proposition 2.1 □

Step 3. Higher order terms. Lastly, we are going to prove that, after large times, the solutions of (22) $p_n^{c,s}(t)$ and $q_n^{c,s}(t)$, with $n > 1$ are periodic with the same period as $x(t)$. We remark again that, since the dynamics of x (23) is independent of p_n^c, p_n^s, q_n^c, q_n^s for $n > 1$, we may assume that $x(t)$ is given and periodic, and split the system into pairs of coupled equations as stated in the following Proposition.

Proposition 2.2 (Higher order coefficients)**.** *For $n > 1$ consider the infinite system of four equations:*

$$\begin{cases} \dot{p_n^c}(t) + \dfrac{2\pi n}{\ell}\dot{x}p_n^s(t) = -a_0(\Omega)p_n^c(t) + a_n(\Omega)/\ell, \\ \dot{p_n^s}(t) - \dfrac{2\pi n}{\ell}\dot{x}p_n^c(t) = -a_0(\Omega)p_n^s(t) + b_n(\Omega)/\ell. \end{cases} \tag{36}$$

and

$$\begin{cases} \dot{q_n^c}(t) - \dfrac{2\pi n}{\ell}\dot{x}q_n^s(t) = -a_0(\Omega)q_n^c(t) + a_n(\Omega)/\ell, \\ \dot{q_n^s}(t) + \dfrac{2\pi n}{\ell}\dot{x}q_n^c(t) = -a_0(\Omega)q_n^s(t) + b_n(\Omega)/\ell. \end{cases} \tag{37}$$

Suppose that, for $t \geq 0$, the function $t \mapsto x(t)$ is periodic of period T. Then, the solutions to the systems (36) *and* (37) *may have two behaviors: they either converge in time to periodic solutions of the same period T if n is odd, or they go to zero for large times when n is even.*

Proof. We introduce $z_n = p_n^c + ip_n^s$. The first two equations of (36) then become:

$$\dot{z}_n + \left(a_0(\Omega) - \frac{2in\pi}{\ell}\dot{x} \right) z_n = c_n \tag{38}$$

where $c_n = \dfrac{a_n(\Omega) + ib_n(\Omega)}{\ell}$ is constant. We thus deduce the following expression for $z_n(t)$

$$z_n(t) = c_n \int_0^t e^{-\int_u^t (a_0(\Omega) - i\bar{v}(s))ds} du + z_n(0) e^{-\int_0^t (a_0(\Omega) - i\bar{v}(s))ds}, \tag{39}$$

where $\bar{v} = \frac{2n\pi}{\ell}\dot{x}$.

Let us first notice that the second term, $z_n(0)e^{-\int_0^t (a_0(\Omega) - i\bar{v}(s))ds}$ goes to zero when t goes to infinity. This, together with the fact that $a_n = b_n = 0$ if n is even (see (3)), gives $c_n = 0$ and the solutions $p_n^{c,s}$ go to zero for large times when n is even.

Let us now focus on the case where n is odd. We want to prove that, when $\bar{v}$ is periodic of period T, z_n converges towards a T-periodic solution after a transitory regime. We again notice that the second term of (39) converges to 0, and the result will follow by studying only the first term.

We thus denote by $\tilde{z}_n(t) = \int_0^t e^{-\int_u^t (a_0 - i\bar{v}(s))ds} du$, and compute

$$\begin{aligned}
\tilde{z}_n(T+t) - \tilde{z}_n(t) &= \int_0^{t+T} e^{-\int_u^{t+T} (a_0 - i\bar{v}(s))ds} du - \int_0^t e^{-\int_u^t (a_0 - i\bar{v}(s))ds} du \\
&= \int_0^T e^{-\int_u^{t+T} (a_0 - i\bar{v}(s))ds} du + \int_T^{t+T} e^{-\int_u^{t+T} (a_0 - i\bar{v}(s))ds} du \\
&\quad - \int_0^t e^{-\int_u^t (a_0 - i\bar{v}(s))ds} du \,.
\end{aligned} \tag{40}$$

Using the fact that $\bar{v}$ is T-periodic, the last two terms cancel and we obtain

$$\begin{aligned}
\tilde{z}_n(T+t) - \tilde{z}_n(t) &= \int_0^T e^{-\int_u^{t+T} (a_0 - i\bar{v}(s))ds} du \\
&= e^{-(t+T)a_0} \int_0^T e^{ua_0 + \int_u^{t+T} i\bar{v}(s)ds} du
\end{aligned}$$

which goes to 0 when t goes to infinity.

We therefore proved that z_n converges to a T-periodic function. The same result holds for (q_n^c, q_n^s) solution to (37). □

Finally, if we have initial conditions that are close to the equilibrium point of system (1), and an amount of ATP Ω, which is close to Ω_0, we know exactly how the solution of the system evolves in time. The first order coefficients of (20) go quickly to the constant term $1/l$, the first order coefficients starts to oscillate in a limit cycle, and the higher order terms either go to zero or have the same patterns as $p_1^{c,s}$ and $q_1^{c,s}$ with same period of oscillation. Globally, the solution of (1), shows a supercritical Hopf-bifurcation in time, close enough to the parameter Ω_0.

Remark 2.1. We remark that, up until the computation of the center manifold, the coefficients a_0, a_1 and b_1 may remain general: there is no need for the power laws to obtain three negative eigenvalues and two complex eigenvalues in system (24). To facilitate the application of center manifold techniques, we have opted to explicitly express the dependence of a_0, a_1, and b_1 on Ω. The selection of power laws is somewhat intuitive, as it extends previous findings ([6],[12]) and proves to be advantageous for our analysis.

2.5 Numerical method

We now describe the numerical scheme used throughout the remaining of the paper.

It is used here to compute the solution to the two-row model (1), but can easily be extended to N-row models, for $N > 2$ or restricted to the 1-row model.

We write a first-order upwind scheme for the densities P and Q where, after each step, we update the velocity v. Let us take Δx such that $\ell = J\Delta x$ for $J \in \mathbb{N}^*$, and Δt the time step. We define $P_j^n := P(j\Delta x, n\Delta t)$ and $Q_j^n := Q(j\Delta x, n\Delta t)$ for $n \geq 1$ and $1 \leq j \leq J$. Being ℓ-periodic, we may extend P_j^n for all $j \in \mathbb{Z}$ by setting $P_{j+J}^n = P_j^n$ for all $j \in \mathbb{Z}$ and all $n \in \mathbb{N}$; the same can be done for Q_j^n. At a fixed time step $t = n\Delta t$, $n \geq 1$, the velocity v^n of the central tubule pair being

known, we compute, for $j \in \mathbb{Z}$

$$\begin{cases} S_j^n = -a_0 P_j^n + \omega_2(j\Delta x)/\ell, \\ T_j^n = -a_0 Q_j^n + \omega_2(j\Delta x)/\ell, \\ P_j^{n+1} = \begin{cases} \left(1 - v^n \dfrac{\Delta t}{\Delta x}\right) + v^n \dfrac{\Delta t}{\Delta x} P_{j-1}^n + \Delta t S_j^n, & \text{if } v^n > 0, \\ \left(1 + v^n \dfrac{\Delta t}{\Delta x}\right) - v^n \dfrac{\Delta t}{\Delta x} P_{j+1}^n + \Delta t S_j^n, & \text{if } v^n < 0, \end{cases} \\ Q_j^{n+1} = \begin{cases} \left(1 + v^n \dfrac{\Delta t}{\Delta x}\right) - v^n \dfrac{\Delta t}{\Delta x} Q_{j-1}^n + \Delta t T_j^n, & \text{if } v^n > 0, \\ \left(1 - v^n \dfrac{\Delta t}{\Delta x}\right) + v^n \dfrac{\Delta t}{\Delta x} Q_{j+1}^n + \Delta t T_j^n, & \text{if } v^n < 0, \end{cases} \end{cases} \tag{41}$$

and $(x^{n+1},\, v^{n+1})$ are

$$\begin{cases} \eta v^{n+1} = \Delta x \sum_{j=1}^{J} \left(\left(P_j^{n+1} - Q_j^{n+1} \right) \partial_\xi \Delta W(j\Delta x) \right) - k x^n, \\ x^{n+1} = x^n + v^{n+1} \Delta t. \end{cases} \tag{42}$$

Notice that, in (41), only one of the two updates is used for all j. Moreover, due to the stability of the upwind scheme, we need to check at each iteration that $\left| v^n \dfrac{\Delta t}{\Delta x} \right| < 1$.

2.5.1 Conditions on α_0 and α_1

Table 1: Values of the parameters used in numerical simulations.

Parameter	Value
ℓ	$10\, nm$
$k_B T$	$4.2668 \cdot 10^{-3}\, nN \cdot nm$
η	$1.0 \cdot 10^{-7}\, kg/s$
k	$9.5 \cdot 10^{-5}\, kg/s^2$
U	$10 k_B T$
a_0^0	$1.0 \cdot 10^{3}\, s^{-1}$
Ω_0	$15 k_B T$

In order to implement the numerical simulations, we have to characterize ω_1 and ω_2 by fixing their coefficients. We first set the values for a_0^0 and Ω_0. For simplicity, we impose that $a_n = b_n = 0$ for $n > 1$ since, as observed in Theorem 1.2, they have no significant influence over the system's oscillations. We now want to find some a_1^0, α_0, α_1, that verify $\tau(\Omega_0) = 0$ from equation (4)

and $\tau'(\Omega_0) > 0$. Starting with α_0 and α_1, we search for sufficient conditions such that $\tau'(\Omega_0) > 0$. This inequality reads

$$\frac{1}{2}a_0^0\alpha_0\Omega_0^{\alpha_0-1} - (\alpha_0-\alpha_1)\frac{\lambda a_1^0}{2a_0^0\ell}\Omega_0^{\alpha_1-\alpha_0-1} < 0,$$

Substituting a_1^0 into it we get

$$a_0^0(2\alpha_0-\alpha_1)\Omega_0^{\alpha_0} + (\alpha_0-\alpha_1)\frac{\ell\zeta}{2\pi} < 0. \tag{43}$$

The condition (43) is fulfilled with different choices for α_0, α_1. A particularly simple solution that we will use hereafter is $\alpha_0 = 1/2$ and $\alpha_1 = 1$. Then, to recover $a_1^0 = a_1^0(\Omega_0)$, we solve $\tau(\Omega_0) = 0$, from equation (4), which leads to

$$a_1^0 = -\frac{a_0^0\ell}{2\pi\lambda}\Omega_0^{\alpha_0-\alpha_1}(2a_0^0\Omega_0^{\alpha_0}\pi + \ell\zeta). \tag{44}$$

Finally, using the parameter values presented in Table 1, we compute a_1^0 at the instability and get $a_1^0(\Omega_0) = -56.4588\, s^{-1}$.

2.6 Numerical simulations

Motivated by the previous computations, all simulations are carried out defining $\Delta W(\xi) = U\cos(2\pi\xi/\ell)$, $a_0(\Omega) = a_0^0\sqrt{\Omega}$, $a_1(\Omega) = b_1(\Omega) = a_1^0\Omega$ and $a_n(\Omega) = b_n(\Omega) = 0$, if $n > 1$, with $\alpha_0 = 1/2$ and $\alpha_1 = 1$. It is fundamental to notice that the choice to define $b_1 \neq 0$, makes the transition rates not-symmetric, as in [12].

All parameters values used for all simulations are shown in Table 1, matching F. Jülicher's [6]. We have taken for k_BT the value at $36°C$ (human body temperature).

As shown in Figure 2, the behavior of the two-row model with respect to the ATP concentration is comparable with the one for the one-row model. When the ATP concentration Ω is lower than Ω_0, the central pair does not move from its zero equilibrium position. On the contrary, when the ATP concentration is high enough, we observe an oscillatory displacement between microtubules and in the probabilities.

The main difference between the one-row model and the two-row one concerns the equilibrium position around which the solution $x(t)$ oscillates, as expected. This is clearly illustrated in Figure 2(b), where the displacement takes place around zero. In this case, the equilibrium position does not create any curvature, meaning it has the potential to bend equally in both directions.

The simulations for the one-row model where carried out using the same upwind numerical scheme. In this case there is only one probability density $P(\xi, t)$. It is linked to the only moving filament, whose displacement is defined as $x(t)$. We used the same notation as the literature, see [6] for example.

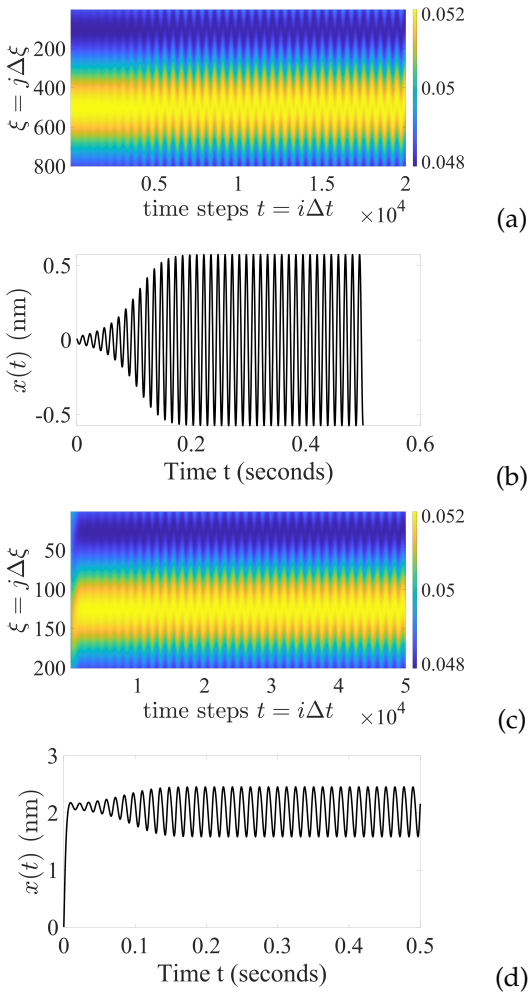

Figure 2: Two-row model ((a),(b)) and one-row model ((c),(d)): (a) Probability density $P_1(\xi, t)$ of the top layer of being in state 1 over time in a periodicity cell, in steady-state regime. The probability density $P_2(\xi, t)$ of the bottom layer of being in state 1 is similar to $P_1(\xi, t)$. (b) Relative tubule shift x over time. (c) Probability density $P(\xi, t)$ of the moving layer in the one-row model. (d) Relative tubule shift x over time in the one-row model.

2.6.1 Illustrating Theorem 1.2

In the following section, we are going to test the results of Theorem 1.2 against numerical simulations of the original partial differential equations system (1) and its first order approximation as the ordinary differential equations system (24).

All constants are chosen as described in Table 1, and in Section 2.5.1. The parameter δ indicates the relative distance from the instability Ω_0; therefore, the point where the simulations is performed is $\Omega_0(1+\delta)$.

Motivated by the previous computations, we numerically solve the ODE (24) and the PDE (1) for $\Omega = \Omega_0(1+\delta)$ with $\delta > 0$, focusing on the amplitude of oscillations for the displacement.

To determine the *numerical amplitude* for both the ODE and the PDE, we calculate the difference between the maximum and minimum values of the solution after some time $\bar{t}$, when the numerical solution has reached its limit cycle. This difference is then divided by two.

We then compare the numerical amplitude with the *theoretical amplitude* defined by (5). For our choice of parameters and neglecting higher-order terms, the theoretical amplitude simplifies to:

$$\rho(\Omega) = \sqrt{\delta \frac{\ell^2}{6\pi^2} \left(\frac{\pi a_0^0 \Omega_0^{1/2} + 2\ell\zeta}{\pi a_0^0 \Omega_0^{1/2} + \ell\zeta} \right)}. \tag{45}$$

In Figure 3, simulations only start after $\delta = 0.05$. This is related to the fact that the closer we are to Ω_0, the slower the solution enters into its limit cycle. For this reason, we should have taken a time $\bar{t} = t(\delta)$ after which evaluating the amplitude of $x(t)$. In this case, when δ goes to zero, $\bar{t}(\delta) \to \infty$. In the simulations this was not reasonable, so we chose a time $\bar{t}$ independently from δ, but large enough so that the solution enters in its steady-state regime for all δs.

In Figure 3(a), we observe the amplitude of $x(t)$ computed with the PDE, the ODE, and the analytical result (45). As expected, the last loses its prediction capability the more we go away from the instability; and subsequently, the relative error between the truncated formula (5) and the one measured from the PDE increases, as we can see in Figure 3(b). This is due to the contribution of the non linear terms, which play a role in determining the amplitude of oscillations even when the system is close to Ω_0.

2.6.2 Comment on the amplitude

The expansion (5) of the amplitude ρ can also be adapted to the ODE formulation of the one-row model. In Figure 4, the two-row model does not only center the equilibrium point for the oscillations around zero, but it also influences important physical quantities such as the amplitude of oscillations.

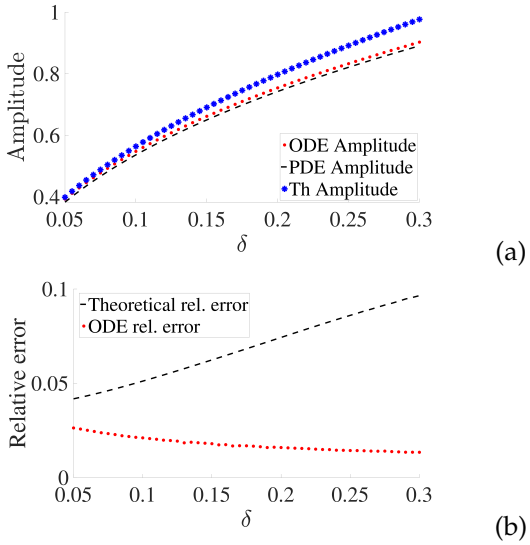

Figure 3: Two-row model. (a) Displacement amplitude vs. relative distance to instability: the red curve shows the amplitude from the ODE (24), the black curve from the PDE (1) and the theoretical amplitude from (45) in blue. (b) Relative error results between the theoretical amplitude and the ODE (in red), and the theoretical amplitude and the PDE (in black).

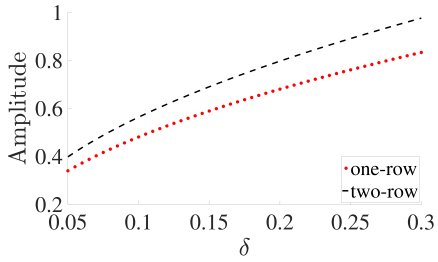

Figure 4: Theoretical amplitude for the 2-row model computed with formula (5) in black and its equivalent for the 1-row model, in red, against the distance from instability δ.

3 Towards modeling the axoneme: N-layer model with fixed extremities

Starting from two rows of molecular motors, we extend the model from section 2 to $N \geq 2$ rows of molecular motors, without any explicit form of inhibition in the system.

The system is then composed of $N + 1$ microtubule doublets on the outside, arranged in a circle, and no central pair. All filaments have the same polarity, meaning that between two microtubule pairs, motors move towards the base.

To take the bridge of an axoneme into account (as shown in Figure 5) in our

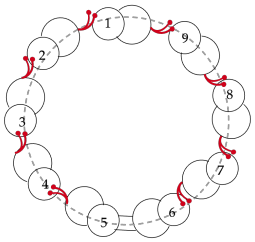

Figure 5: Simplified axoneme with 9 microtubule doublets and no central pair [31]. Note the presence of a bridge between pairs 5 and 6.

N-layer model, filament pairs 0 and N are considered to be the same pair. They have no shift between each other, as shown in the split view Figure 6. Moreover, all microtubule pairs are assumed inextensible, rigid and at a constant distance from each other. They are held together by elastic and viscous elements that do not permit infinite sliding between them. We look at molecular motors in a periodicity cell of an N-axoneme, of length ℓ.

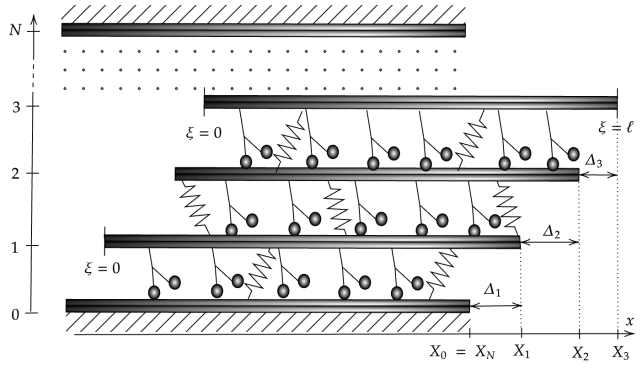

Figure 6: Motors and tubule shift in the N-row model (here the horizontal axis x shows absolute tubule displacement instead of motor position ξ in a periodicity cell).

3.1 Full mathematical model

For $i \in \{0, \dots, N\}$, we denote by X_i the horizontal shift of the i-th tubule, as shown in Figure 6. We measure displacement with respect to the 0-th filament: $X_0 = X_N = 0$. For $1 \leq i \leq N$, we introduce $\Delta_i = X_i - X_{i-1}$, the relative displacement between filaments i and $i-1$. It follows that $\sum_{i=1}^{N} \Delta_i(t) = 0$. The shifting speed of the i-th filament is defined by $V_i = \dot{X}_i - \dot{X}_{i-1} = \dot{\Delta}_i$, and we

have

$$\sum_{i=1}^{N} V_i = \sum_{i=1}^{N} \dot{\Delta}_i(t) = 0. \tag{46}$$

Once again, the variable $\xi \in [0, \ell]$ represents the local variable along one pair, as in the two-row model. We denote by $Q_i(\xi, t)$ the density of molecular motors at position ξ and time t attached to the i-th filament and who are in state 1, walking on the $(i-1)$-th filament.

As for the two-row model, in section 2, $(Q_i,\, \Delta_i)$ are solution to, for $\xi \in [0, \ell]$ and $t > 0$

$$\begin{cases} \partial_t Q_j(\xi, t) = -(\omega_1(\xi - \Delta_j(t), t) + \omega_2(\xi - \Delta_j(t)))Q_j(\xi, t) \\ \qquad\qquad + \omega_2(\xi - \Delta_j(t)))/\ell, \quad \text{for } j \in \{1, \dots, N\}, \\ \eta(V_i(t) - V_{i+1}(t)) = \displaystyle\int_0^\ell (Q_i(\xi, t)\partial_\xi \Delta W(\xi) - Q_{i+1}(\xi, t)\partial_\xi \Delta W(\xi - \Delta_i(t)))d\xi \\ \qquad\qquad - k(\Delta_i(t) - \Delta_{i+1}(t)), \quad \text{for } i \in \{1, \dots, N-1\}. \end{cases} \tag{47}$$

Where the first equation is a transport equation for the motors probability density. Shifting speed is measured by looking at the current filament, as well as the one above. We thus obtain the second equation in system (47) by writing the force balance on the i-th filament with the motors and springs around it. We then have $N-1$ force-balance equations that determine the filaments' motion, in which we impose the external forces to be zero.

Following again section 2, for $j \in \{1, \dots, N\}$, $t > 0$ and $\xi \in [0, \ell]$, we define P_j as $P_j(\xi, t) = Q_j(\xi + \Delta_j(t), t)$. We then observe that $\partial_t P_j(\xi + \Delta_j, t) = V_j(t)\partial_\xi Q_j(\xi, t) + \partial_t Q_j(\xi, t)$, and we finally obtain the system at any $t > 0$ and $\xi \in [0, \ell]$

$$\begin{cases} \partial_t P_j + V_j \partial_\xi P_j = -(\omega_1 + \omega_2)P_j + \omega_2/\ell, \qquad \text{for } j \in \{1, \dots, N\}, \\ \eta(V_i - V_{i+1}) = \displaystyle\int_0^\ell (P_i - P_{i+1})\partial_\xi \Delta W - k(\Delta_i - \Delta_{i+1}), \quad \text{for } i \in \{1, \dots, N-1\}, \\ \qquad\qquad \displaystyle\sum_{i=1}^{N} \dot{\Delta}_i(t) = 0 \text{ and } \dot{X}_n = 0. \end{cases} \tag{48}$$

Like in previous models, the equilibrium state is, for all $1 \le i \le N-1$ and $1 \le j \le N$

$$\begin{cases} V_i = 0, \\ X_i = 0, \\ P_j = P^0 = \dfrac{\omega_2}{\ell(\omega_1 + \omega_2)}. \end{cases}$$

3.2 Theoretical considerations

In this situation we want to investigate the existence of a Hopf bifurcation in time, as it was done with the two-row model. To do so, we consider a linearized system arising from the N-row model (48), in order to have a general idea of the system's dynamics, as in (20). We expand in Fourier series $P_1, \dots, P_N$ and treat order by order the Fourier coefficients of the probabilities. For the first order coefficients, we obtain a $3N-1$ dimensional ODE system with unknowns:

$$p_j^{c,s}, \quad j = 1, \dots, N, \qquad X_k,\ k = 1, \dots, N-1.$$

We then perform some linear change of variables, similarly to (2.4), in order to write the Jacobian of the system as a block matrix. The first block is a $N+1$ diagonal matrix with real and negative entries $-a_0(\Omega)$. The rest of the linearized system is defined by the following equations

$$\begin{pmatrix} \dot{q}_k \\ \dot{w}_k \end{pmatrix} = \begin{pmatrix} -\frac{2\pi^2}{\ell\eta} U p_e - a_0 & -\frac{2\pi}{\ell\eta} k p_e \\ -\pi U/\eta & -k/\eta \end{pmatrix} \begin{pmatrix} q_k \\ w_k \end{pmatrix} \tag{49}$$

for $k = 1, \dots, N-1$, where $p_e = a_1/(a_0\ell)$, $q_k = p_k^s - p_{k+1}^s$ for $k = 1, \dots, N-1$, and

$$\begin{pmatrix} w_1 \\ \vdots \\ w_{N-1} \end{pmatrix} = \begin{pmatrix} 2 & -1 & & & \\ -1 & 2 & -1 & & \\ & & \ddots & & \\ & & -1 & 2 & -1 \\ & & & -1 & 2 \end{pmatrix} \begin{pmatrix} X_1 \\ \vdots \\ X_{N-1} \end{pmatrix}. \tag{50}$$

It follows that the Jacobian has $N+1$ real and negative eigenvalues $-a_0(\Omega)$, and $N-1$ identical pairs of complex and conjugated ones $\mu_k(\Omega)$ for $k = 1, \dots, N-1$ which come from (49). We observe that $\mu_k(\Omega) = \tau(\Omega) + i\omega(\Omega)$, with τ and ω defined as in Theorem 1.2 by equations (4) and (25). Then, if there exists $\Omega = \Omega_0$ such that $\tau(\Omega_0) = 0$ and $\tau'(\Omega_0) > 0$, the eigenvalues cross the imaginary axis all at the same bifurcation parameter. Thus, there is a suggestion of a bifurcation in the dynamics at Ω_0, indicated by the linear part of the complete dynamical system. We will not investigate the theoretical aspects of this model further in this paper, as the Central Manifold Theorem used in previous section, does not apply to such systems. However, as shown in the next section, numerical simulations still suggest a potential pattern in the oscillations and hint that there is indeed a bifurcation.

3.3 Numerical results

In this section, the N-layer model is tested for $N = 8$, to match the 8 motor rows of an axoneme with a bridge and nine microtubule doublets, as in Figure 5. We use the same parameter values as for the previous systems, as specified in Table 1. The initial conditions are such that $P_i(t=0) = P^0$ for all i, and we destabilize the X_is randomly in $[-x_0, x_0]$, where $x^0 = 0.01\,nm$.

Using the same notations as before, i.e. $\Omega = (1+\delta)\Omega_0$, we measure distance the to the bifurcation point Ω_0 using δ.

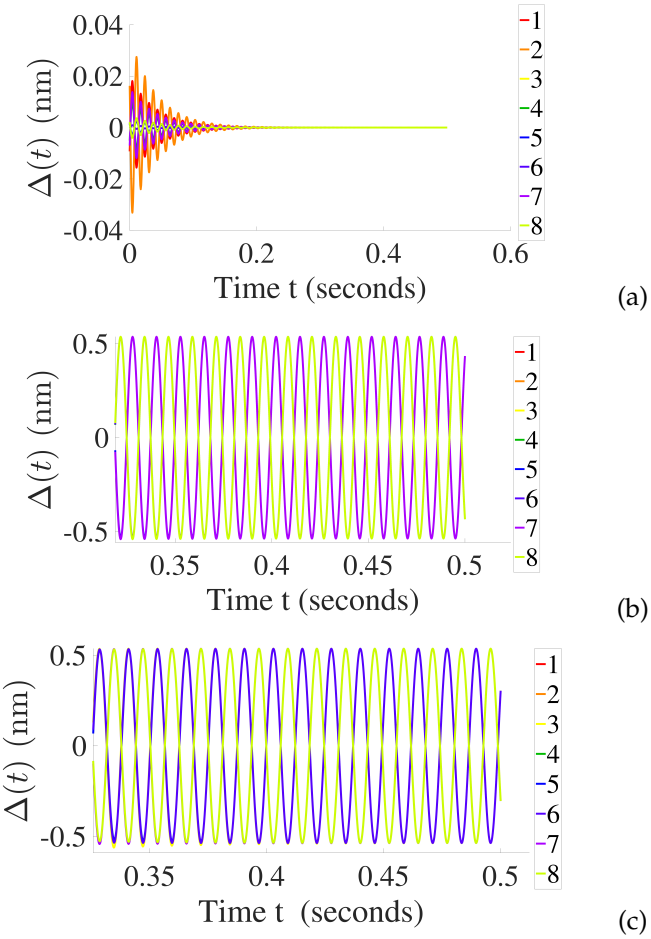

Figure 7: N-row model ($N = 8$). Relative tubule displacement (in nm) with respect to time (in seconds) for random initial conditions (a) before bifurcation point, for $\delta = -0.1$ ($\Omega = 0.9\Omega_0$) and (b) and (c) after bifurcation point , for $\delta = 0.1$ ($\Omega = 1.1\Omega_0$), for two iterations of random initial conditions.

Figure 7(a) shows the absence of oscillations before instability ($\Omega = 0.9\Omega_0$), exactly as expected. Even though the system is put out of equilibrium by the initial conditions, since some tubule shifts are nonzero, they all quickly go back to zero and stop moving.

In Figure 7(b), we look at the system past the instability point, for $\Omega = 1.1\Omega_0$. Here, the system clearly reaches a steady-state oscillating regime after a short amount of time. All oscillations also remain centered in zero. As expected from the linear study in section 3.2, all Δ_is have the same amplitude and oscillation

frequency, but their phase difference varies depending on initial conditions. In the particular case shown in Figure 7(b), one group of tubule pairs is synchronized with pair 7, and the other group with pair 8. In fact, when looking at all layers separately, one can see that odd layers (respectively even layers) oscillate in sync. The other possible outcome when running the simulation with random initial conditions was groups $\{1,\ 2,\ 7,\ 8\}$ and $\{3,\ 4,\ 5,\ 6\}$ oscillating together, as shown in Figure 7(c). This influence of the initial conditions is understandable since there is no external force taking the whole axonemal structure and filament into account, resulting in limited coupling between layers at this level. The layers thus tend to keep their original phase difference. The synchronization shown in Figure 7(c) was predicted by Howard et al. [13], and proves the importance of having a bridge around which the system alternates between positive and negative displacement. In the general case, since there is no theory behind the bifurcation of this system of $3N-1$ equations, formally understanding the coupling between phase difference and initial conditions remains an open question.

A similar problem has recently been numerically studied in Kuramoto oscillators [1]. The Kuramoto model is fairly different from ours, as each oscillator has its own velocity, whereas all of our layers have one common velocity value. Our system of equations cannot thus be easily reduced to a Kuramoto model, but the behaviors of the two systems in terms of synchronization and dependence on initial conditions are very much alike. Some first steps, only modelling individual motors along a single row, have been presented in [8].

4 Conclusion and outlook

In this paper, we presented a new model for the axoneme, the cytoskeleton of cilia and flagella, focusing on the presence of spontaneous oscillations and potential synchronization of microtubule doublets under varying ATP concentrations. We called this model N-row model, where N represents the number of rows of motors walking between two microtubule doublets that are arranged in a circular configuration. Molecular motors are put into motion thanks to a chemical reaction involving ATP, thus inducing microtubule sliding. This specific structural arrangement results in all microtubule doublets having a zero equilibrium position. The dynamic is governed by N transport equations, coming from a stochastic two-state model, and $N-1$ force balance equations, collectively forming a PDE system with $2N-1$ equations. We analyzed this model using both theoretical methods and numerical simulations. Our first studies focused on the $N=2$ configuration, revealing the existence and uniqueness of the displacement solution. Moreover, under sufficient chemical energy, the middle microtubule doublet exhibits spontaneous oscillations, corresponding to the existence of a super-critical Hopf-bifurcation in the dynamical system. Theoretical results are corroborated by numerical simulations. Subsequently, we conduct numerical analysis of the N-row model, focusing particularly on the case $N=8$. Here too, we observe that the system starts to oscillate once the ATP

concentration surpasses a critical threshold. Remarkably, under appropriate initial conditions, we note the emergence of two out-of-phase groups among the microtubules, oscillating around the zero position with opposite shifting directions.

The first result on our model can be appreciated starting from the $N = 2$ case. The cylindrical structure answers the problem of the axonemal symmetrization proposed in [6], previously solved by choosing symmetric transition rates. Instead, in of this paper, asymmetric transition rates have been used all along. More in general, even in the N-row model, we observed that the equilibrium displacement with null external force was zero, independently from the potentials and the transition rates. This means that the desired symmetry of the axoneme is always preserved: at equilibrium, with no external forces, each microtubule has the same role and there is no initial shifting in the structure. We underline that this is made possible in our model without imposing specific symmetry for the potentials.

From a more theoretical point of view, both Theorem 1.1 (well-posedness) and Theorem 1.2 (existence of a Hopf bifurcation) give a complete mathematical description on the two-row model. The same results can be proven for the one-row model as well, formalizing the work done in [12]. With the N-row model with fixed extremes, we set up a framework that is useful to gain insights on the microscopic structure of the axoneme. In particular, we comment on the specific case $N = 8$, which is the closest representation of the real axoneme in terms of number of microtubule doublets. With the aid of the numerical scheme presented in the two-row model section, we observed the onset of oscillations at a critical value of ATP. To perturb the system we tried several random initial conditions. We then noticed that imposing an opposite shift on each half of the model immediately led to robust and realistic patterns, potentially leading to planar flagellar beating patterns, as discussed in [19].

A natural extension to our work would be to take into account the presence of the central microtubule pair and, therefore, of the radial spokes coming from outer doublets towards the axonemal center. Moreover, this model can be thought of as a building block that, coupled with mechanics of an elastic flagellum, gives the feedback that generates oscillatory patterns following in the footsteps of [7, 21] and [28] for the planar case and of [23] for the three dimensional case.

Funding

This work was supported by a public grant as part of the Investissement d'avenir project, reference ANR-11-LABX-0056-LMH, LabEx LMH.

A Center manifold computation

In practice, equation (31) is a system of three equations. With the first equation below we aim to find the coefficients a_{1j}, with $j = 1, \dots, 6$

$$
\begin{aligned}
(2a_{11}y + a_{12}x + a_{13}\delta\Omega\,) \Bigg(& -a_0^0\Omega_0^{\alpha_0}y - \frac{\lambda}{\ell}\frac{a_1^0}{a_0^0}\Omega_0^{\alpha_1-\alpha_0}y - \frac{a_1^0}{a_0^0}\frac{\zeta}{\ell}\Omega_0^{\alpha_1-\alpha_0}x \\
& -a_0^0 c(\alpha_0)\delta\Omega\; y - \frac{\lambda}{\ell}\frac{a_1^0}{a_0^0}c(\alpha_1-\alpha_0)\delta\Omega\; y - \frac{\zeta}{\ell}c(\alpha_1-\alpha_0)\delta\Omega\; x \\
& - \frac{b_1^0(r+s-2z)}{2a_1^0}(\zeta x + \lambda y)\Bigg) \\
& + (a_{12}y + 2a_{14}x + a_{15}\delta\Omega\,)(-\frac{\beta\ell}{2\pi}y - \frac{\alpha\ell}{2\pi}x) \\
& + a_0^0\Omega_0^{\alpha_0}h_1 + a_0^0 c(\alpha_0)\delta\Omega\; h_1 \\
& - (\zeta x + \lambda y)\left(\frac{(a_1^0)^2(y+z) + (b_1^0)^2(-r+y+z)}{a_1^0 b_1^0}\right) = 0.
\end{aligned}
$$

Since we only need terms x, y and $\delta\Omega$ up to order two, we get rid of all the third order terms, getting

$$
\begin{aligned}
(2a_{11}y + a_{12}x + a_{13}\delta\Omega\,) \Bigg(& -a_0^0\Omega_0^{\alpha_0}y - \frac{\lambda}{\ell}\frac{a_1^0}{a_0^0}\Omega_0^{\alpha_1-\alpha_0}y - \frac{a_1^0}{a_0^0}\frac{\zeta}{\ell}\Omega_0^{\alpha_1-\alpha_0}x\Bigg) \\
& + (a_{12}y + 2a_{14}x + a_{15}\delta\Omega\,)(-\frac{\beta\ell}{2\pi}y - \frac{\alpha\ell}{2\pi}x) \\
& + a_0^0\Omega_0^{\alpha_0}h_1 - (\zeta x + \lambda y)\left(\frac{(a_1^0)^2 y + (b_1^0)^2 y}{a_1^0 b_1^0}\right) = 0.
\end{aligned} \tag{51}
$$

We then proceed by matching the terms x, y and $\delta\Omega$ with same order, and solve the resulting system of equations for a_{1j}. Notice we could have kept only the zero order term in the Taylor expansion, since all the higher order terms disappear during this approximation.

We do the same for the second and third equation, solving for the power series of h_2 and h_3.

For $i = 1, 2$, we obtain

$$
\begin{aligned}
a_{i1} &= -\frac{2\pi^2\lambda^2 a_0^0\ell\left((a_1^0)^2 + (b_1^0)^2\right)\Omega_0^{\alpha_1-\alpha_0}}{b_1^0\left(2\pi a_1^0\lambda\Omega_0^{\alpha_1-\alpha_0} + \zeta a_0^0\ell^2\right)\left(2\pi a_1^0\lambda\Omega_0^{\alpha_1-\alpha_0} + a_0^0\ell(\pi a_0^0\Omega_0^{\alpha_0} - \zeta\ell)\right)} \\
a_{i2} &= \frac{2\pi\zeta(a_0^0)^2\ell^2\left((a_1^0)^2 + (b_1^0)^2\right)(\zeta l - \pi a_0^0\Omega_0^{\alpha_0})}{a_1^0 b_1^0\left(2\pi a_1^0\lambda\Omega_0^{\alpha_1-\alpha_0} + \zeta a_0^0\ell^2\right)\left(2\pi a_1^0\lambda\Omega_0^{\alpha_1-\alpha_0} + a_0^0\ell(\pi a_0^0\Omega_0^{\alpha_0} - \zeta\ell)\right)} \\
a_{i3} &= 0, \quad a_{i4} = -\frac{2\pi^2\zeta^2 a_0^0\ell\left((a_1^0)^2 + (b_1^0)^2\right)\Omega_0^{\alpha_1-\alpha_0}}{b_1^0\left(2\pi a_1^0\lambda\Omega_0^{\alpha_1-\alpha_0} + \zeta a_0^0\ell^2\right)\left(2\pi a_1^0\lambda\Omega_0^{\alpha_1-\alpha_0} + a_0^0\ell(\pi a_0^0\Omega_0^{\alpha_0} - \zeta\ell)\right)} \\
a_{i5} &= 0, \quad a_{i6} = 0.
\end{aligned}
$$

For $i = 3$ we get

$$a_{31} = -\frac{2\pi^2\lambda^2 a_0^0 b_1^0 \ell \Omega_0^{\alpha_1-\alpha_0}}{\left(2\pi a_1^0\lambda\Omega_0^{\alpha_1-\alpha_0} + \zeta a_0^0\ell^2\right)\left(2\pi a_1^0\lambda\Omega_0^{\alpha_1-\alpha_0} + a_0^0\ell(\pi a_0^0\Omega_0^{\alpha_0} - \zeta\ell)\right)}$$

$$a_{32} = \frac{2\pi\zeta c^2 b_1^0\ell^2(\pi a_0^0\Omega_0^{\alpha_0} - \zeta\ell)}{a_1^0\left(2\pi a_1^0\lambda\Omega_0^{\alpha_1-\alpha_0} + \zeta a_0^0\ell^2\right)\left(2\pi a_1^0\lambda\Omega_0^{\alpha_1-\alpha_0} + c\ell(\pi a_0^0\Omega_0^{\alpha_0} - \zeta\ell)\right)}$$

$$a_{33} = 0, \quad a_{34} = -\frac{2\pi^2\zeta^2 a_0^0 b_1^0 \ell \Omega_0^{\alpha_1-\alpha_0}}{\left(2\pi a_1^0\lambda\Omega_0^{\alpha_1-\alpha_0} + \zeta a_0^0\ell^2\right)\left(2\pi a_1^0\lambda\Omega_0^{\alpha_1-\alpha_0} + a_0^0\ell(\pi a_0^0\Omega_0^{\alpha_0} - \zeta\ell)\right)}$$

$$a_{35} = 0, \quad a_{36} = 0.$$

References

[1] A. Bayani, S. Jafari, H. Azarnoush, F. Nazarimehr, S. Boccaletti, and M. Perc. Explosive synchronization dependence on initial conditions: The minimal kuramoto model. Chaos Soliton. Fract., 169:113243, 2023.

[2] P. V. Bayly and S. K. Dutcher. Steady dynein forces induce flutter instability and propagating waves in mathematical models of flagella. J. R. Soc. Interface, 13(123):20160523, 2016.

[3] C. J. Brokaw. Flagellar Movement: A Sliding Filament Model: An explanation is suggested for the spontaneous propagation of bending waves by flagella. Science, 178(4060):455–462, 1972.

[4] C. J. Brokaw. Bending patterns of ATP-reactivated sea urchin sperm flagella following high salt extraction for removal of outer dynein arms. Cell. Motil. Cytoskel., 42(2):125–133, 1999.

[5] C. J. Brokaw. Computer simulation of flagellar movement X: Doublet pair splitting and bend propagation modeled using stochastic dynein kinetics. Cytoskeleton, 71(4):273–284, 2014.

[6] S. Camalet and F. Jülicher. Generic aspects of axonemal beating. New J. Phys., 2(1):324, 2000.

[7] J. Cass and H. Bloomfield-Gadêlha. The reaction-diffusion basis of animated patterns in eukaryotic flagella. Nat. Commun., 14, 09 2023.

[8] G. Costantini and A. Puglisi. Thermodynamic precision of a chain of motors: the difference between phase and noise correlation. J. Stat. Mech.: Theory Exp., 2024(2):024003, feb 2024.

[9] E. Gaffney, H. Gadêlha, D. Smith, J. Blake, and J. Kirkman-Brown. Mammalian sperm motility: Observation and theory. Annu. Rev. Fluid Mech., 43(1):501–528, 2011.

[10] E. A. Gaffney, K. Ishimoto, and B. J. Walker. Modelling motility: The mathematics of spermatozoa. Front. Cell Dev. Biol., 9, 2021.

[11] J. Gray and G. J. Hancock. The propulsion of sea-urchin spermatozoa. J. Exp. Biol., 32, 1955.

[12] T. Guérin, J. Prost, and J.-F. Joanny. Dynamical behavior of molecular motor assemblies in the rigid and crossbridge models. Eur. Phys. J. E, 34:1–21, 2011.

[13] J. Howard, A. Chasteen, X. Ouyang, V. F. Geyer, and P. Sartori. Predicting the locations of force-generating dyneins in beating cilia and flagella. Front. Cell Dev. Biol., 10, 2022.

[14] T. Hu and P. V. Bayly. Finite element models of flagella with sliding radial spokes and interdoublet links exhibit propagating waves under steady dynein loading. Cytoskeleton, 75(5):185–200, 2018.

[15] F. Jülicher, A. Ajdari, and J. Prost. Modeling molecular motors. Rev. Mod. Phys., 69:1269–1282, 1997.

[16] F. Jülicher and J. Prost. Cooperative molecular motors. Phys. Rev. Lett., 75:2618–2621, 1995.

[17] F. Jülicher and J. Prost. Spontaneous oscillations of collective molecular motors. Phys. Rev. Lett., 78:4510–4513, 1997.

[18] F. Jülicher and J. Prost. Molecular Motors: From Individual to Collective Behavior. Prog. Theor. Phys. Supp., 130:9–16, 1998.

[19] C. B. Lindemann and K. A. Lesich. The many modes of flagellar and ciliary beating: Insights from a physical analysis. Cytoskeleton, 78(2):36–51, 2021.

[20] K. E. Machin. Wave Propagation along Flagella. J. Exp. Biol., 35(4):796–806, 1958.

[21] D. Oriola, H. Gadêlha, and J. Casademunt. Nonlinear amplitude dynamics in flagellar beating. R. Soc. Open Sci., 4(3):160698, 2017.

[22] E. M. Purcell. Life at low Reynolds number. Am. J. Phys., 45(1):3–11, 01 1977.

[23] P. Sartori, V. F. Geyer, J. Howard, and F. Jülicher. Curvature regulation of the ciliary beat through axonemal twist. Phys. Rev. E, 94:042426, Oct 2016.

[24] P. Sartori, V. F. Geyer, A. Scholich, F. Jülicher, and J. Howard. Dynamic curvature regulation accounts for the symmetric and asymmetric beats of *Chlamydomonas* flagella. eLife, 5:e13258, 2016.

[25] K. E. Summers and I. R. Gibbons. Adenosine triphosphate-induced sliding of tubules in trypsin-treated flagella of sea-urchin sperm. Proc. Nat. Acad. Sci. USA, 68(12):3092–3096, 1971.

[26] G. I. Taylor. Analysis of the swimming of microscopic organisms. Proc. R. Soc. Lond. A, 209:447–461, 1951.

[27] M. F. Velho Rodrigues, M. Lisicki, and E. Lauga. The bank of swimming organisms at the micron scale (boso-micro). PLoS One, 16(6):1–80, 06 2021.

[28] B. J. Walker, S. Phuyal, K. Ishimoto, C.-K. Tung, and E. A. Gaffney. Computer-assisted beat-pattern analysis and the flagellar waveforms of bovine spermatozoa. R. Soc. Open Sci., 7(6), 2020.

[29] S. Wiggins. Springer, Texts in Applied Mathematics. 2003.

[30] L. G. Woodhams, Y. Shen, and P. V. Bayly. Generation of ciliary beating by steady dynein activity: the effects of inter-filament coupling in multi-filament models. J. R. Soc. Interface, 19(192):20220264, 2022.

[31] T. Yagi and R. Kamiya. Novel mode of hyper-oscillation in the paralyzed axoneme of a chlamydomonas mutant lacking the central-pair microtubules. Cell Motil., 31(3):207–214, 1995.